AGU PUBLICATIONS

JGR

Journal of Geophysical Research: Oceans

RESEARCH ARTICLE

10.1002/2016JC012404

Turbulent kinetic energy of the ocean winds over the Kuroshio Extension from QuikSCAT winds (1999–2009)

Kai Yu[1,2,3], Changming Dong[1,4], and Gregory P. King[1,5,6]

[1]Oceanic Modeling and Observation Laboratory, School of Marine Science, Nanjing University of Information Science and Technology, Nanjing, China, [2]State Key Laboratory of Satellite Ocean Environment Dynamics, Second Institute of Oceanography, State Oceanic Administration, Hangzhou, China, [3]Jiangsu Research Center for Ocean Survey Technology, Nanjing, China, [4]Institute of Geophysics and Planetary Physics, University of California, Los Angeles, California, USA, [5]Institut de Ciències del Mar (ICM-CSIC), Passeig Marítim Barceloneta, Barcelona, Spain, [6]Centro de Geofisica-IDL, Universidade de Lisboa, Lisboa, Portugal

Key Points:
- Spatial variance characterizes TKE better than the second-order structure function
- TKE over the Kuroshio Extension has a strong seasonal cycle and correlates with El Niño 3.4 index
- Results imply downscale energy cascade with nonclassical features and strong monthly fluctuations

Correspondence to:
G. P. Kind,
gking.lisboa@outlook.com;
C. Dong,
cmdong@gmail.com

Citation:
Yu, K., C. Dong, and G. P. King (2017), Turbulent kinetic energy of the ocean winds over the Kuroshio Extension from QuikSCAT winds (1999–2009), *J. Geophys. Res. Oceans*, *122*, 4482–4499, doi:10.1002/2016JC012404.

Received 6 OCT 2016
Accepted 12 MAR 2017
Accepted article online 13 APR 2017
Published online 1 JUN 2017

Abstract We investigate mesoscale turbulence (10–1000 km) in the ocean winds over the Kuroshio Extension (28°N–40°N, 140°E–180°E) using the QuikSCAT data set (November 1999 to October 2009). We calculate the second (D_{jj}) and third-order structure functions (D_{jjj}) and the spatial variance (V_j) as a function of scale r ($j=L, T$ denotes, respectively, the longitudinal (divergent) and transverse (vortical) component). The most interesting results of the analysis follow. Although both $V_j(r)$ and $D_{jj}(r)$ measure the turbulent kinetic energy (*TKE*), we find that $V_j(r)$ is the more robust measure. The spatial variance density (dV_j/dr) has a broad peak near 450 km (close to the midlatitude Rossby radius of deformation). On interannual time scales, *TKE* correlates well with the El Niño 3.4 index. According to turbulence theory, the kinetic energy cascades downscale (upscale) if $D_{LLL}(r)$ (also skewness $S_L=D_{LLL}/D_{LL}^{3/2}$) is negative (positive). Our results for the Kuroshio Extension are consistent with a downscale cascade (indicating convergence dominates). Furthermore, classical turbulence theory predicts that $S_L=-0.3$ and independent of r; however, we find S_L varies strongly with r, from -4 at small scales to -0.3 at large scales. This nonclassical behavior implies strong-scale interaction, which we attribute to the rapid, and sometimes explosive, growth of storms in the region through baroclinic instability. Finally, we find that S_T (a measure of cyclonic/anticyclonic asymmetry) is positive (cyclonic) and also varies strongly with r, from 4 at small scales to 0.5 at large scales. New turbulence models are needed to explain these results, and that will benefit Weather Prediction and climate modeling.

Plain Language Summary The turbulent winds near the ocean surface give rise to air-sea heat and momentum exchange. The turbulence is caused by convective processes -- processes generated at weather fronts, in squalls, tropical disturbances and extra-tropical cyclones. In order to improve forecasts and climate models of such weather systems, it is necessary to improve physical models of the turbulence, for which satellite observations are crucial. In this paper we analyze ten years of satellite observed winds over the Kuroshio Extension, a region well-known for its vigorous air-sea heat and momentum exchange and storm generation. We document the seasonal and interannual variations in the turbulent kinetic energy amplitude and its scaling. Our results also reveal strong and intermittent turbulent features that are not found in current theories and models of the surface winds, thus indicating directions for new modelling strategies.

1. Introduction

The Kuroshio Current, carries warm ocean waters northward from the tropics along the western boundary of the Pacific Ocean and, on reaching Japan, is deflected eastward deep into the Central Pacific. The contrast between the warm core of the Kuroshio and adjacent waters gives rise to a strong ocean front with a sea surface temperature (SST) gradient of approximately 10°C over just 200 km [see the review by *Kelly et al.*, 2010, and references therein]. Furthermore, instabilities in the fast moving, meandering Kuroshio creates ocean eddies with steep SST gradients, generating low-level baroclinicity. The atmospheric instability caused by high Kuroshio SST combines with low-level baroclinicity to bring high momentum wind from the free-troposphere down to the ocean surface. These processes generate strong ocean winds and turbulence and increase synoptic storm activity, making the Kuroshio Extension a

site of vigorous air-sea heat and momentum exchange [*Wyrtki et al*., 1976; *Tai and White*, 1990; *Qiu*, 1995; *Yu and Weller*, 2007; *Booth et al*., 2010; *Kelly et al*., 2010].

Global forecast models, both weather and climate, do not resolve convective processes; instead they rely on parameterizating them to make useful forecasts. On the other hand, satellite scatterometers reveal small-scale (i.e., mesoscales: 2–2000 km) information in the ocean winds missed by global forecast models [*Vogelzang et al*., 2011]. Characterizing turbulence in the mesoscales is important, for it is the range of scales where weather fronts, mesoscale convective systems, tropical disturbances, and extratropical cyclones are found. Hence it is critically important for weather and climate modeling to understand the characteristics of the turbulence statistics in this range of scales and how they vary regionally and over time. Such information is necessary for building improved parameterizations for use in Numerical Weather Prediction (NWP) and climate models.

Statistical methods developed in the theory of turbulence provide a critical link between the forecast models and observations. These are the energy spectrum and the structure functions (the moments of the probability distribution of velocity increments). The energy spectrum and the second-order structure function are related by the Fourier transform (for conditions satisfied by atmospheric turbulence), with the emphasis normally being on the scaling exponent of the turbulence. However, emphasis on scaling overlooks the importance of the amplitude of the kinetic energy fluctuations (hereafter turbulent kinetic energy *TKE*). This may partly be explained as due to the lack of a direct correspondence between the *TKE* estimated from the spectrum with the *TKE* estimated from the second-order structure function [cf., *Davidson and Pearson*, 2005]. In a recent paper, *Vogelzang et al*. [2015] reintroduced the spatial variance, a statistical quantity that provides an exact relation between the sample variance and second-order structure function. The spatial variance provides a different link to the energy spectrum, as well as solving another difficulty—how to represent the distribution of *TKE* in real space as the spectrum is purported to do in wavenumber space.

The principle objective of this paper then is to build a regional history of the statistics of low-level turbulent activity, including statistics that characterize the energy transfer between small and large-scales, using the database of QuikSCAT winds. The SST fronts, free-tropospheric storm tracks, low-level winds, and their interaction over the Kuroshio Extension exhibit prominent seasonal and interannual variability [*Qiu*, 2000; *Zhu and Sun*, 1999; *Tokinaga et al*., 2006; *Tanimoto et al*., 2009]. It can be expected that this variability will be reflected in the turbulence statistics, which will be useful in modeling (parameterizations) that represent subgrid processes in weather and climate models.

The remainder of this paper is organized as follows. Section 2 introduces the notation and theoretical relationships for structure functions and spatial variance used in this paper. Section 3 describes the data and methodology. In section 4, we present our results for the mean state and the seasonal and interannual variability of the turbulence in the ocean winds over the Kuroshio Extension. In section 5, we discuss our results and give our conclusions.

2. Structure Functions and Spatial Variance

We follow the notation and definitions used in *King et al*. [2015a,2015b] and *Vogelzang et al*. [2015].

2.1. Velocity Increments and Structure Functions

The Kolmogorov theory of turbulence is developed in terms of velocity increments [cf., *Frisch*, 1995]. Let $\delta\vec{u}=\vec{u}(\vec{x},\vec{r})-\vec{u}(\vec{x})$ be the velocity increment between the pair of points $\vec{x}+\vec{r}$ and $\vec{x}$. If the probability distribution of $\delta\vec{u}$ is invariant under translations, reflections, and rotations of such pairs of points, it follows that $\delta\vec{u}(\vec{x},\vec{r})$ is a homogeneous and isotropic field (i.e., the field $\vec{u}(\vec{x})$ is locally homogeneous and locally isotropic).

In a coordinate system based on the configuration of measured points, the axis parallel to $\vec{r}$ is denoted by L (the longitudinal direction, but *not* the longitude), and the two statistically equivalent directions normal to $\vec{r}$ by T (transverse direction). The distance between points along the L axis is denoted by r. Note that the L, T notation is standard in the turbulence literature. For the conditions holding in ideal turbulence, the first three moments of the probability distribution of velocity increments $P(\delta u_j, r)$, $j=L,T$, are

$$\delta U_j = \langle \delta u_j \rangle = 0, \tag{1}$$

$$D_{jj} = \langle \delta u_j \delta u_j \rangle, \tag{2}$$

$$D_{jjj} = \langle \delta u_j \delta u_j \delta u_j \rangle \tag{3}$$

where the angle brackets denote ensemble averages.

The second-order longitudinal structure function follows an $r^{2/3}$ scaling law for both ideal 2-D turbulence (forced at both small and large-scales) [*Lindborg*, 1999] and ideal 3-D turbulence:

$$D_{LL}(r) = C_{Ld} |\varepsilon_d|^{2/3} r^{2/3} \tag{4}$$

where C_{Ld} is a universal constant ($C_{L3} \approx 2$ and $C_{L2} \approx 12$) and ε_d is the rate of energy dissipation.

For ideal incompressible turbulence, the divergence equation yields a relation between $D_{TT}(r)$ and $D_{LL}(r)$, which can be written for d-dimensional turbulence as [cf., *Lindborg*, 1999],

$$D_{TT}(r) = D_{LL}(r) + \frac{r}{d-1} D_{LL}(r). \tag{5}$$

From equation (5), it follows that D_{TT} has the same scaling law as D_{LL} when the turbulence is homogeneous and isotropic.

When D_{LL} and D_{TT} follow power laws, the ratio of vorticity-to-divergence varies according to whether turbulence is 2-D or 3-D:

$$\frac{D_{TT}}{D_{LL}} = \begin{cases} \frac{5}{3} & (\text{2D}), \\ \frac{4}{3} & (\text{3D}). \end{cases} \tag{6}$$

Note also that in the case of turbulence generated by gravity waves, *Lindborg* [2007] shows that $D_{TT}/D_{LL} = 3/5$.

Kolmogorov showed that in the small-scales of ideal 3-D turbulence the cascade of energy from large to small-scales leads to the third-order longitudinal structure function relation

$$D_{LLL}(r) = -\frac{4}{5} \varepsilon_3 r \qquad (\text{3D}), \tag{7}$$

where $\varepsilon_3 > 0$. *Lindborg* [1999] extended the analysis to 2-D turbulence and showed that

$$D_{LLL}(r) = \frac{3}{2} \varepsilon_2 r \qquad (\text{2D}) \tag{8}$$

with the sign of ε_2 indeterminate so that if $\varepsilon_2 > 0$, then $D_{LLL}(r) > 0$ and energy transfer is upscale, but if $\varepsilon_2 < 0$, then $D_{LLL}(r) < 0$ and energy transfer is downscale.

The skewness of $P(\delta u_j, r)$ is defined by

$$S_j(r) = \frac{D_{jjj}(r)}{[D_{jj}(r)]^{3/2}} \tag{9}$$

For the longitudinal component, turbulence theory predicts that

$$S_L(r) = \begin{cases} -0.3 & \text{if 3D (downscale energy transfer)}, \\ +0.03 & \text{if 2D (upscale energy transfer)}. \end{cases} \tag{10}$$

In geophysical terms, because the third-order moments measure the asymmetry in the distribution of velocity increments, the Kolmogorov-Lindborg theories make predictions about the asymmetry between convergence and divergence. Regarding the third-order transverse structure function, it describes the asymmetry between cyclonic and anticyclonic vorticity. However, at present there are no theoretical predictions for it.

2.2. Spatial Variance

Vogelzang et al. [2015] rediscovered the *spatial variance*—a relationship between the ensemble averaged sample variance $V_j(r)$ and the second-order structure function $D_{jj}(r)$. They derived the following relationships:

$$V_j(r) = \frac{1}{r^2}\int_0^r (r-s)D_{jj}(s)\,ds \tag{11}$$

$$D_{jj}(r) = \left(r^2\frac{d^2}{dr^2} + 4r\frac{d}{dr} + 2\right)V_j(r) \tag{12}$$

$V_j(r)$ measures the cumulative *TKE* over a scale r. The energy contained in a range of scales (r_1, r_2) is therefore

$$\Delta V_j(r_1, r_2) = V_j(r_2) - V_j(r_1), \tag{13}$$

which can be written as an integral from r_1 to r_2 of the derivative of $V_j(r)$. From equation (11) it is straightforward to show that

$$\frac{d}{dr}V_j(r) = \frac{1}{r^3}\int_0^r (2s-r)D_{jj}(s)\,ds. \tag{14}$$

This shows that $dV_j(r)/dr$ can be interpreted as a variance density in position space, which implies that a peak appearing in a plot of $dV_j(r)/dr$ versus r can be interpreted as a preferred scale for turbulent eddies. [see *Vogelzang et al.*, 2016 for an illustration of the use of the variance density to diagnose and model a noise peak in the ASCAT 6.25 km wind product.]

2.3. Relations Between Spectra, Structure Functions, and Spatial Variance

The second-order structure function $D_{jj}(r)$ and the energy spectrum $E_j(k)$ are related through the extended Wiener-Khinchin formula [*Frisch*, 1995]:

$$D_{jj}(r) = 2\int_0^\infty (1-\cos kr)E_j(k)\,dk. \tag{15}$$

Clearly, substituting the right-hand side of equation (15) for D_{jj} in equation (12) yields a relation between $V_j(r)$ and $E_j(k)$.

It follows from equation (15) and the finiteness of energy, that if $D_{jj}(r) \sim r^\beta$ with $0 < \beta < 2$, then the spectrum follows the scaling $E_j(k) \sim k^{-\beta-1}$. Thus if $D_{jj}(r) \sim r^{2/3}$ then $E_j(k) \sim k^{-5/3}$ and if $D_{jj}(r) \sim r^2$ then $E_j(k) \sim k^{-3}$.

When D_{jj} follows a simple power law, $D_{jj}(r) = Cr^{-p}$, with C a constant, substitution into equation (11) or (12) yields

$$V_j(r) = \frac{Cr^p}{(p+1)(p+2)} \tag{16}$$

which leads to

$$\frac{V_j(r)}{D_{jj}(r)} = \frac{1}{(p+1)(p+2)} \tag{17}$$

so that if the exponent $p = 2/3$,1 or 2, then, respectively, $V_j/D_{jj} = 0.225$, 1/6, or 1/12.

The relationship expressed in equation (17) is validated using data produced by an algorithm simulating fractional Brownian motion in Appendix A.

3. Data and Methodology

The QuikSCAT satellite was launched by the National Aeronautics and Space Administration (NASA) into a quasi-sun-synchronous orbit with an inclination angle of 98.62°, a period of 101 min (14.5 orbits/d), a recurrent period of 4 days, and local equatorial crossing times at about 06:00 for the ascending pass (South to North) and 18:00 for the descending pass (North to South). The SeaWinds scatterometer is a rotating pencil-beam design with an 1800 km swath and operates at Ku-band at 13.4 GHz [*Tsai et al.*, 2000].

3.1. Data

The QuikSCAT winds used in this study are the rain-corrected winds selected by the Direction Interval Retrieval with Threshold Nudging algorithm provided in the QSCAT-12.5 (version 3) Level 2B product from the NASA Jet Propulsion Laboratory (JPL). The DIRTH rain-correction algorithm estimates a rain impact for each wind vector cell, and whenever this quantity exceeds a threshold, a rain speed correction is applied [*Fore et al.*, 2014]. We also use the National Center for Environmental Prediction (NCEP) global forecast winds included in this data product. The NCEP winds are interpolated to the same latitude, longitude, and time as the QuikSCAT wind. The data set begins in late October 1999 and ends mid-November 2009; however, we only use winds during the ten year period 1 November 1999 through 31 October 2009. Wind vectors are presented in an along-track/cross-track swath grid of wind vector cells (WVCs), which are square 12.5 km-by-12.5 km pixels.

We also use a gridded product from Remote Sensing Systems (RSS) to investigate the climatological mean wind and its seasonal variability: The RSS QuikSCAT Ku-2011 Monthly Ocean Vector Winds on 0.25° grid, Version 4 [*Ricciardulli et al.*, 2011].

3.2. Methodology

3.2.1. Kuroshio Extension Study Area

Figure 1 shows the Kuroshio Extension and adjacent areas. The study area is defined as the area between the two horizontal black lines drawn at 28°N and 40°N, and between longitudes 140°E and 180°E. Superimposed on both Figures 1a and 1b are the climatological mean wind vectors. These show that the study region lies between a zone of westerly winds to its north and easterly trade winds to its south. Between these is a jet-like feature of convergent wind that angles slightly northward (Figure 1a). There is strong wind shear ($\partial u/\partial y$) at the edge of both boundaries of this jet-like feature, producing cyclonic vorticity to the north and anticyclonic vorticity to the south (Figure 1b).

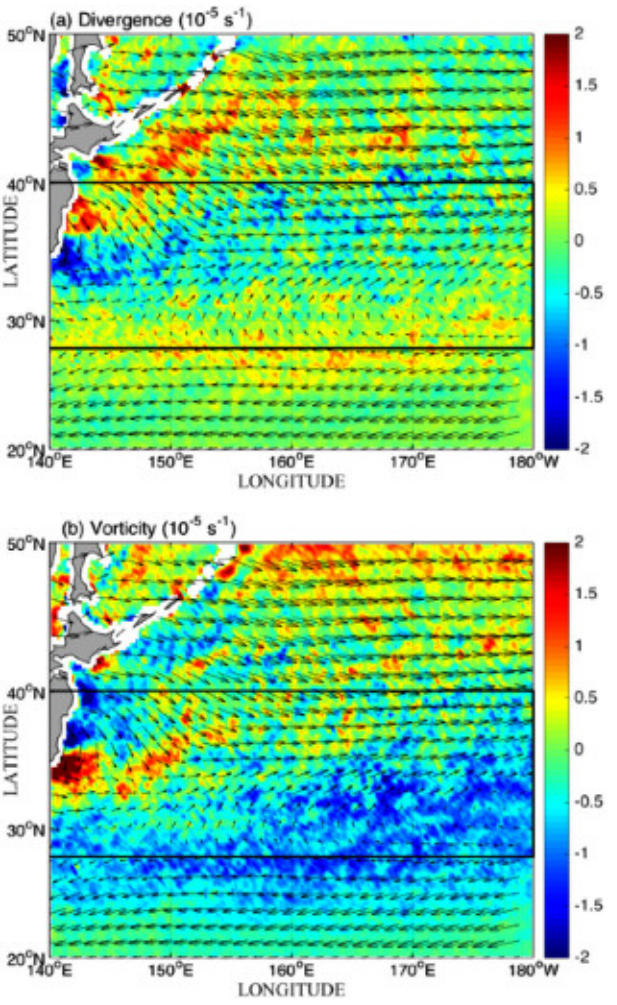

Figure 1. The Kuroshio Extension, showing the climatological mean wind superimposed on (top) the divergence field and (bottom) vorticity field (units: s^{-1}) derived from the gridded RSS QuikSCAT product. Along-track samples are selected between latitudes 28°N and 40°N (indicated by the black horizontal lines) and between longitudes 140°E and 180°E.

3.2.2. Grid Description

The QuikSCAT data are organized into files, where a single data file with no measurement gaps gives full coverage of the earth's circumference (one complete orbit). In each file, the WVCs and their data are organized into a matrix with 3248 rows and 152 columns. Each WVC row corresponds to a single cross-track cut of the QuikSCAT measurement swath. Thus the row number gives the along-track position and the column number gives the cross-track position.

The nominal instrument measurement swath extends 900 km to either side of the nadir track with no nadir gap. As an artifact of the orbital inclination and instrument swath width, consecutive orbits will usually start to overlap poleward of ~47° latitude. Further details can be found in the QuikSCAT documentation directory at ftp://podaac.jpl.nasa.gov/allData/quikscat/L2B12/docs.

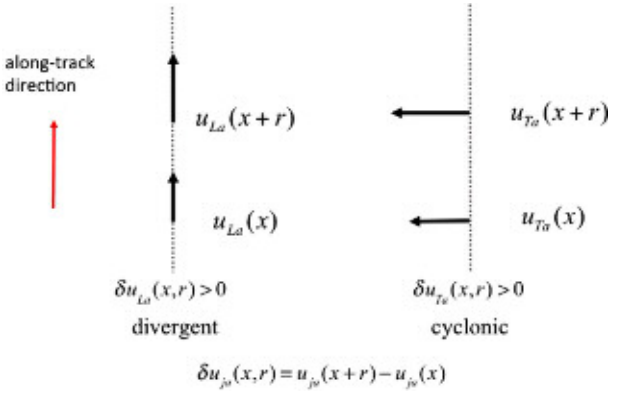

Figure 2. Definition sketch showing the along-track, cross-track coordinate system $(\hat{a},\hat{c})$, and the coordinate system defined by the structure function analysis: $(\hat{L},\hat{T})$. The (L, T) coordinate system is defined so that the local vertical is positive upward: $\hat{z}=\hat{L}\times\hat{T}$. Velocity components in the $(\hat{L},\hat{T})$ coordinate system with $\hat{L}$ and $\hat{a}$ aligned are denoted by u_{ja} and their increments by $\delta u_{ja}=u_{ja}(x_L+r,x_T)-u_{ja}(x_L,x_T)$, where $j=L,T$ and (x_L, x_T) are coordinates in this frame of reference. Positive longitudinal increments indicate divergence, and positive transverse increments indicate cyclonic shear.

3.2.3. Wind Components

The QuikSCAT ocean wind vectors are supplied as wind speed and wind direction. These were transformed into wind components parallel (u_{La}) and perpendicular (u_{Ta}) to the satellite ground track. Note that the subscript a indicates that the L-axis is aligned with the satellite ground track, where positive $\hat{L}$ is in the direction of satellite motion—see Figure 2. The L and T axes are oriented so that the local vertical direction points upward: $\hat{z}=\hat{L}\times\hat{T}$.

The transformation to components u_{La} and u_{Ta} was carried out as follows: first, wind speed (W) and wind direction (in the oceanographic convention, ϕ_o) were transformed to zonal and meridional components (u, v):

$$\phi_u=\pi/2-\phi_o \tag{18}$$

$$u=W\cos\phi_u \tag{19}$$

$$v=W\sin\phi_u \tag{20}$$

In order to transform (u, v) to cross-track and along-track components (u_c, u_a), the angle at which WVC rows are inclined relative to the equatorial plane must be calculated. Using spherical trigonometry, it can be shown that this angle is given by

$$\alpha=\left|\arctan\left(\frac{1}{\cos\phi\tan\Theta}\right)\right|, \tag{21}$$

where ϕ is the latitude and $\Theta=98.62^\circ$ is the QuikSCAT satellite inclination angle. (For a more accurate method to calculate α, see *Vogelzang and Verhoef* [2014].) α is always positive so that the ascending pass (satellite moving South-to-North) is inclined at angle α and the descending pass (satellite moving North-to-South) at angle $-\alpha$. Having calculated α, a coordinate rotation yields

$$u_c=u\cos\theta_p+v\sin\theta_p \tag{22}$$

$$u_a=-u\sin\theta_p+v\cos\theta_p \tag{23}$$

where

$$\theta_p=\begin{cases}\alpha & (\text{ascending pass})\\ \pi-\alpha & (\text{descending pass})\end{cases} \tag{24}$$

Finally, requiring $\hat{z}$ to point vertically upward, the components (u_{La}, u_{Ta}) are:

$$u_{La}=u_a \tag{25}$$

$$u_{Ta}=-u_c \tag{26}$$

3.2.4. Sample Selection

Wind vectors with latitudes and longitudes within the study area were extracted from the QuikSCAT data set. Only along-swath samples were used: i.e., each member of a sample had the same cross-track WVC index. Each sample was checked to ensure wind vectors falling outside the study area were flagged missing. Samples from both the ascending and descending passes and from the whole swath (including the outer and nadir parts) were used to calculate structure functions and spatial variance.

Ku-band radar is sensitive to rain [*Weissman et al.*, 2012]. In the tropics where winds are light and rain heavy, the backscatter signal is heavily corrupted and hence often rejected. In midlatitudes, however, rain does not have as strong an effect on wind quality [*Booth et al.*, 2010]. Therefore, calculations were carried out using both *rain-free* winds (rain-flagged WVCs rejected) and *all-weather* winds (rain-flag ignored).

3.2.5. Calculation Framework

Here we introduce a common framework for the calculation of both structure functions and spatial variances.

Consider a column of WVCs from a given data file. Denote the length of the set of contiguous WVCs with the same WVC index and that lie within the boundaries of the study area by $\mathcal{L}=\ell\Delta r$ ($\Delta r=12.5$ km). Note that $\mathcal{L}$ varies across the swath due to the satellite orbit inclination and shape of the study area. Further note that possibly there will be segments from both the ascending and descending portions of the swath. The number of samples of length $r=n\Delta r \leq \mathcal{L}$ that can be constructed from this set equals $\ell-n+1$. Repeat this for every data file in the range of dates considered for an ensemble average. Denote the total number of such samples by m and each sample by $z_i(r), i=1\ldots m$. These are collected and copied into a data matrix $\mathbf{Z}(r)$, which has size $m\times(n+1)$ (a sample of length r contains $n+1$ points):

$$\mathbf{Z}(r)=\begin{bmatrix} z_{10} & z_{11} & \cdots & z_{1j} & \cdots & z_{1n} \\ \vdots & \vdots & \ddots & \vdots & \ddots & \vdots \\ z_{i0} & z_{i1} & \cdots & z_{ij} & \cdots & z_{in} \\ \vdots & \vdots & \ddots & \vdots & \ddots & \vdots \\ z_{m0} & z_{m1} & \cdots & z_{mj} & \cdots & z_{mn} \end{bmatrix} \tag{27}$$

Note that in calculations, sample members whose WVCs did not pass quality control or lay outside the study region are flagged as missing.

The set of velocity increments for the ensemble are obtained by taking the difference between the first and last columns of $\mathbf{Z}(r)$:

$$\{\delta z_i(r)\}=\{z_{in}-z_{i0}\}, \qquad i=1,\ldots,m. \tag{28}$$

Empirical probability distributions $P(\delta z, r)$ are then constructed from the increments, whose first moment (mean increment at scale r) is easily calculated:

$$\overline{\delta Z}(r)=\frac{1}{m}\sum_{i=1}^{m}\delta z_i(r). \tag{29}$$

The qth-order *centered* structure functions are calculated using

$$D_q(r)=\frac{1}{m}\sum_{i=1}^{m}(\delta z_i(r)-\overline{\delta Z}(r))^q, \qquad q=2,3,\ldots \tag{30}$$

Next, the spatial variance at scale r is calculated as follows:

1. first, the sample mean:

$$\bar{z}_i(r)=\frac{1}{n+1}\sum_{j=0}^{n}z_{ij}, \tag{31}$$

2. then the sample variance:

$$\sigma_k^2(r)=\frac{1}{n+1}\sum_{j=0}^{n}(z_{ij}-\bar{z}_i(r))^2, \tag{32}$$

3. and finally, the spatial variance:

$$V(r)=\frac{1}{m}\sum_{i=1}^{m}\sigma_i^2(r). \tag{33}$$

The calculation framework was applied separately to each wind component u_{ja}, $j=L,T$ to produce the empirical pdfs $P(\delta u_{ja}, r)$, the mean velocity increments $\delta U_{ja}(r)$, the centered structure functions $D_{jja}(r)$ and $D_{jjja}(r)$, and the spatial variances $V_{ja}(r)$.

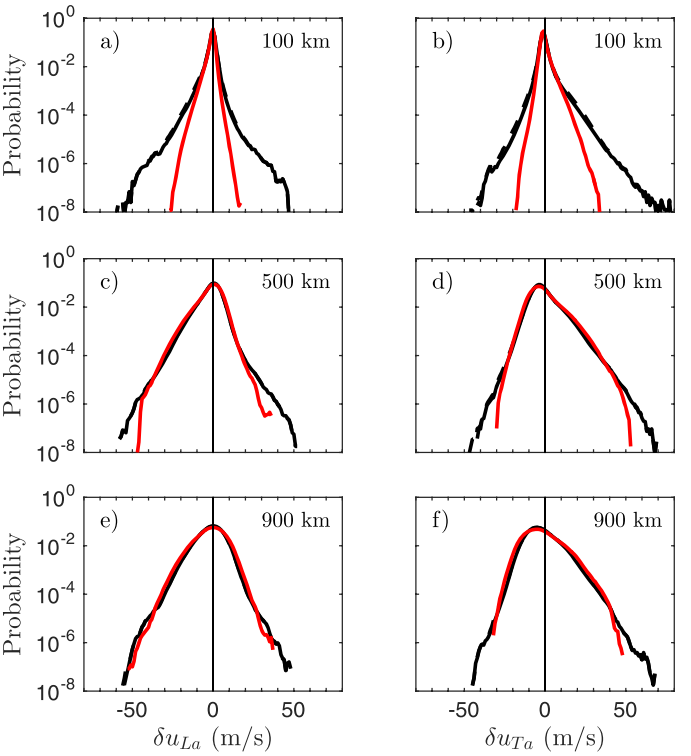

Figure 3. Empirical probability distributions (left) $P(\delta u_{La}, r)$ and (right) $P(\delta u_{Ta}, r)$ constructed using all samples selected from the Kuroshio Extension study area during the 10 year period November 1999 to October 2009: rain-free winds (solid), all-weather (dashed), and NCEP (red) at r = (top) 100 km, (middle) 500 km, and (bottom) 900 km.

While the statistical relationships between D_{jj} and V_j given in section 2 are exact, due to sampling differences and missing data they only approximately hold for the scatterometer data: Samples with missing data have larger uncertainty, and samples whose initial or final component is missing contributes to the spatial variance but not to the structure function. *Vogelzang et al.* [2015] compared different sampling strategies and found that rejecting samples whose initial or final component was missing had a minor effect on the final results. Following these authors, we use all samples that contain at least two points and weight each sample by $w=(n-M)/n$, where $n+1$ is the number of points and M the number of missing points in the sample.

4. Results

4.1. Velocity Increment pdfs

Figure 3 shows velocity increment probability distributions (pdfs) $P(\delta u_{ja}, r)$ constructed from the entire 10 years of QuikSCAT data for rain-free and all-weather conditions at three scales: 100 km (top), 500 km (middle) and 900 km (bottom). In contrast to the heavy rain areas in the tropical Pacific [*King et al.*, 2015a,2015b], rain has only a small effect on the midlatitude pdfs. Therefore, in the remainder of this paper only the results for all-weather winds will be shown.

Figure 3 shows that the pdfs are skewed and have tails that are close to exponential (with positive and negative δu_{ja} having different slopes). The skewness will be described in more detail below, but a study of the tails, whose character and behavior yield important information about extreme events in the Kuroshio extension ocean winds, is outside the scope of the present paper and deferred to a future work.

Figure 3 also shows velocity increment pdfs for the NCEP winds. NCEP pdfs are much narrower than the QuikSCAT pdfs at the smallest scales, only a little narrower by 500 km, and almost the same by 900 km. The pdfs provide a vivid demonstration of how much the NCEP forecast winds miss small-scale extreme events.

The velocity increment pdfs are not always centered at zero. That is, the first-order structure functions, $\delta U_{La}(r)$ and $\delta U_{Ta}(r)$, slowly vary with r, as shown in Figure 4. Both $\delta U_{La}(r)$ and $\delta U_{Ta}(r)$ are negative (i.e., convergent and anticyclonic), reflecting the atmospheric dynamics as well as the geographical limits of the study area (see Figure 1).

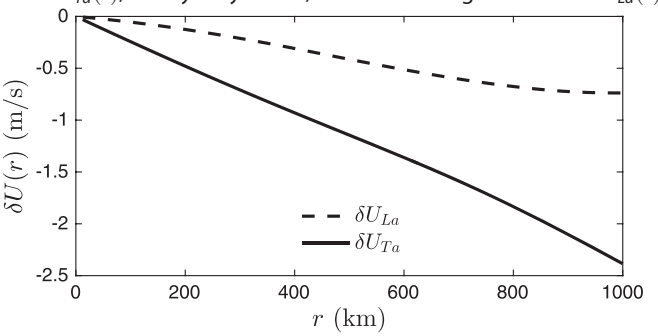

Figure 4. First-order structure functions averaged over all 10 years of the all-weather QuikSCAT winds (units: m/s): δU_{La} (dashed line) and δU_{Ta} (solid line).

4.2. Second-Order Statistics: Structure Functions and Spatial Variances

4.2.1. Mean State

In section 2, it was shown that it should make no difference whether the second-order structure function or the spatial variance is used to study

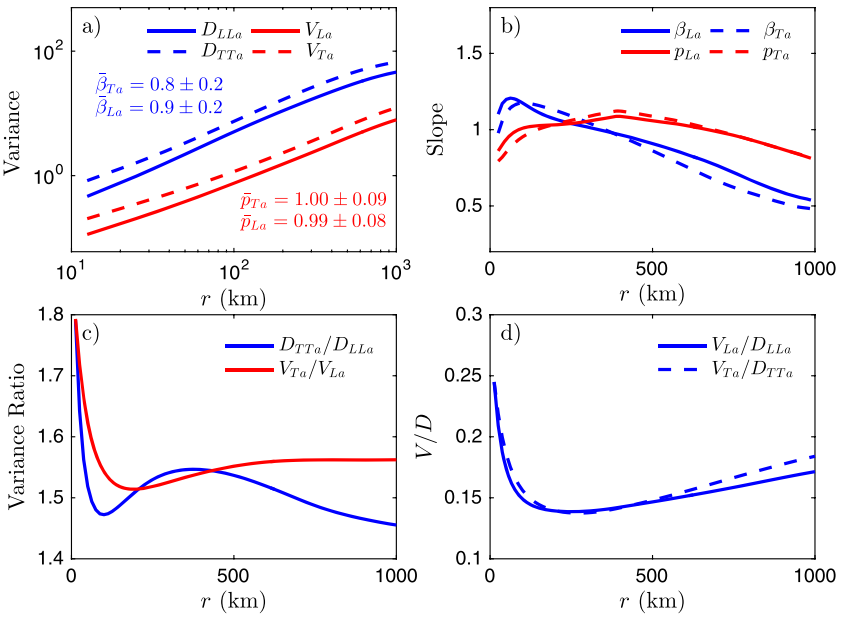

Figure 5. Second-order statistics for the 10 year ensemble of all-weather winds: (a) centered second-order structure functions $D_{LLa}(r)$ and $D_{TTa}(r)$ and spatial variances $V_{La}(r)$ and $V_{Ta}(r)$. (b) Scale-dependent slopes $\beta_{ja}(r)$ and $p_{ja}(r)$ calculated using a sliding three-point fit. The mean slopes are $(\bar{\beta}_{La}, \bar{\beta}_{Ta}) = (0.9, 0.8) \pm (0.2, 0.2)$ and $(\bar{p}_{La}, \bar{p}_{Ta}) = (0.99, 1.00) \pm (0.08, 0.9)$. (c) Vorticity-to-divergence ratios $D_{TTa}(r)/D_{LLa}(r)$ and $V_{Ta}(r)/V_{La}(r)$. (d) Ratio of spatial variance and second-order structure function $V_{La}(r)/D_{LLa}(r)$ and $V_{Ta}(r)/D_{TTa}(r)$.

the distribution and scaling of *TKE*. But in practice, are there advantages to using one rather than the other?

Figure 5 compares (centered) structure functions D_{LLa} and D_{TTa} with spatial variances V_{La} and V_{Ta} calculated using all 10 years of the QuikSCAT data set. Recall that centered structure functions are calculated using adjusted velocity increments: $\delta\tilde{u}_{ja}(r) = \delta u_{ja}(r) - \delta U_{ja}(r)$, where $\delta U_{ja}(r)$ is the ensemble mean velocity increment. In principle, the D_{jja} and V_{ja} power law slopes should all be the same. Figure 5a shows that while this is a good approximation, there is a weak r-dependence. A least squares fit yields structure function slopes $(\bar{\beta}_{La}, \bar{\beta}_{Ta}) = (0.9, 0.8) \pm (0.2, 0.2)$ and spatial variance slopes $(\bar{p}_{La}, \bar{p}_{Ta}) = (0.99, 1.00) \pm (0.08, 0.09)$. The weak r-dependence is identified using a three-point sliding fit (Figure 5b). As can be seen in Figures 5a and 5b, a flatter slope turns to a steeper slope at about 50 km. The flatter slope at scales less than 50 km is due to the noise that remains in the wind vectors after processing [see *Fore et al.*, 2014, section 3C]. From about 100 km, the structure function exponents decrease monotonically from about 1.1 to about 0.5. In contrast, spatial variance exponents rise to a broad maximum (∼1.1) between 400 and 500 km, and then slowly decrease to about 0.8. Clearly the spatial variance follows a power law better than the structure function. This must be due to the

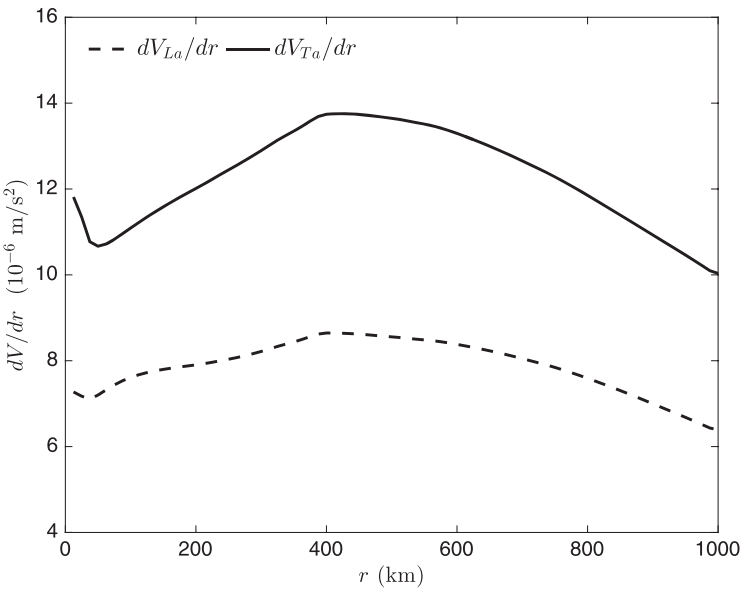

Figure 6. The mean kinetic energy density averaged over all 10 years of the QuikSCAT all-weather winds (units: m/s^2): dV_{La}/dr (dashed line) and dV_{Ta}/dr (solid line).

fact that for a sample of length r consisting of $n+1$ points, the spatial variance uses n data while the structure function uses 2 (i.e., only the sample end points). Hence, as r increases, the amount of information used to calculate the spatial variance as compared to the structure function grows as $n/2$.

The vorticity-to-divergence ratios D_{TTa}/D_{LLa} and V_{Ta}/V_{La} are compared in Figure 5c. The two ratios stay reasonably close at all scales, and for $r > 100$ km stay between 1.45 to 1.55—midway between the values predicted by 2-D and 3-D turbulence theories (respectively, 4/3 and 5/3).

Equation (17) predicts that at sufficiently large r, the ratio V/D equals $1/(p+1)(p+2)$. Figure 5d shows the V/D ratios for both the longitudinal and transverse components. Since the slopes vary with r, we compare the ratios at two scales. From Figure 5b, $p \approx 1$ at 400 km and $p \approx 0.7$ at 1000 km. This yields V/D ratios of about 0.17 and 0.22, respectively. This is in good agreement with the V/D ratios shown in Figure 5d.

In summary, we have found that the spatial variance provides the same information as the second-order structure function and in fact is statistically more robust. Therefore, in the remainder of this paper the spatial variance is used to represent *TKE*. Furthermore, recall that *Vogelzang et al.* [2015] showed that the energy contained between scales r and $r + dr$ is dV/dr. In other words, just as the energy spectrum is the energy density in wavenumber space, dV/dr is the energy density in position space. This means that a peak occurring in a plot of dV/dr vs r has the same interpretation as a peak in the energy spectrum: a preferred length-scale. The graphs of dV_{La}/dr and dV_{Ta}/dr in Figure 6 show two peaks—one near $r = 0$, which we attribute to the noise discussed above [see also *Vogelzang et al.*, 2016], and a broad peak between 400 and 500 km. Interestingly, the scale at which this peak occurs is of the same order as expected for the Rossby deformation radius; this requires further study.

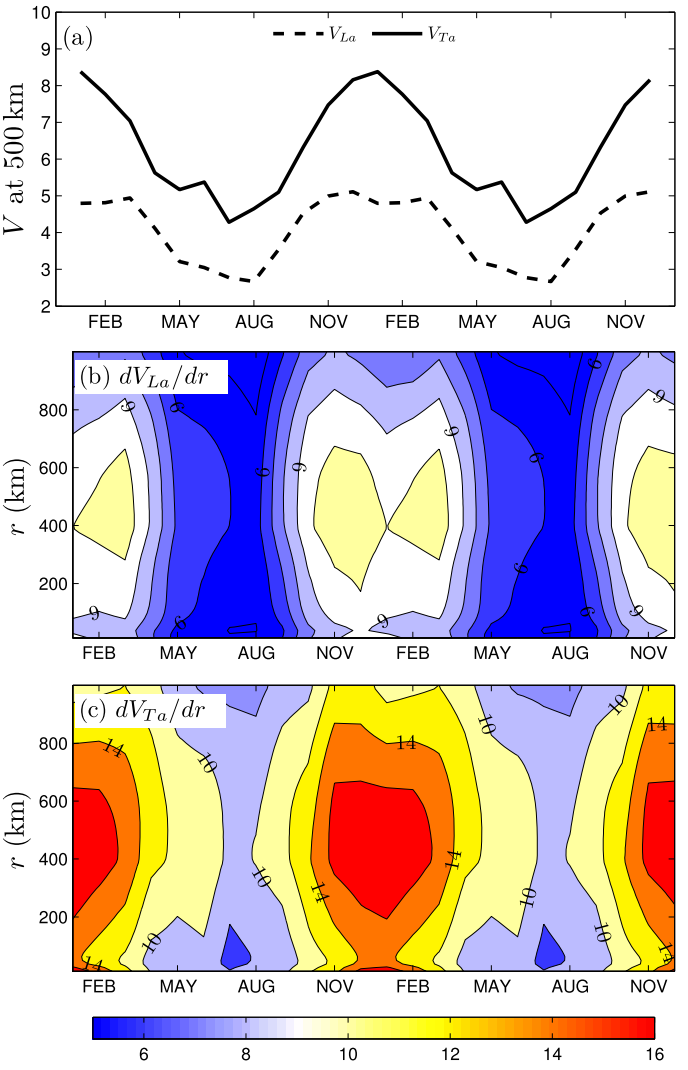

Figure 7. Seasonal variability of the spatial variance (V) and spatial variance density (dV/dr density) over the Kuroshio Extension region: (a) V_{La} and V_{Ta} at 500 km (units: m^2/s^2); (b) dV_{La}/dr_{La}; and (c) dV_{Ta}/dr (units: m/s^2).

4.2.2. Seasonal Variability

Figure 7 shows the seasonal cycles of spatial variance V at 500 km (top) and the spatial variance density dV/dr (middle and bottom). V has the same seasonal cycle as the wind kinetic energy (Figure 8a): larger in winter due to the stronger atmospheric activity in that season [see also *Patoux and Brown*, 2001]. Besides, a local minimum in mid-winter can be clearly seen in dV_{La}/dr (Figure 7b) and less so in dV_{Ta}/dr (Figure 7c). However, the mid-winter minimum does not appear in the seasonal cycle of wind kinetic energy (Figure 8a). That may be due to the seasonal variability of the wind shear, which is considered to be the important factor in the conversion between kinetic energy and *TKE*. Figure 8b, which shows that the zonal wind shear is larger in winter, but moves south across 28°N and out of the study area in November, causes a drop in the *TKE*. Then in late winter

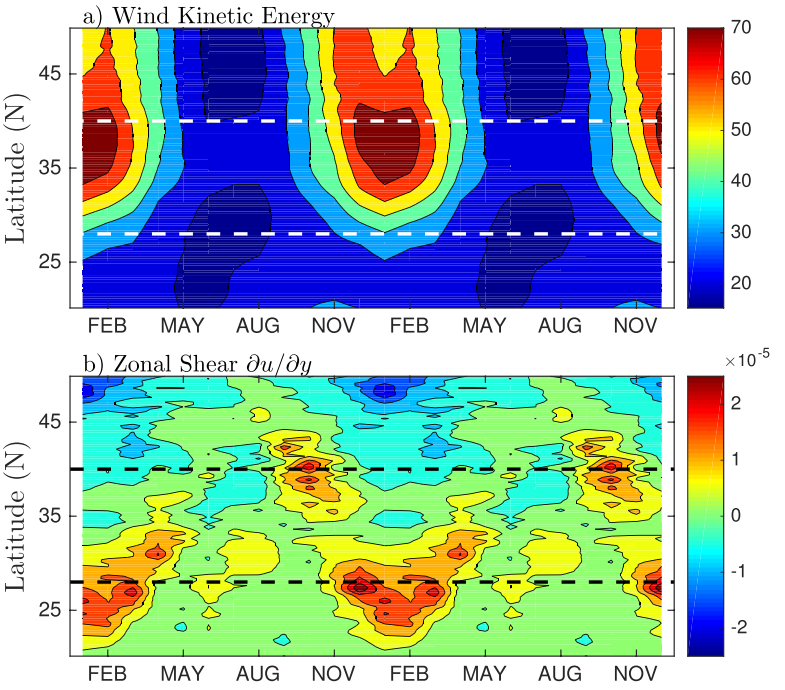

Figure 8. Latitude-seasonal cycle of the (a) zonally averaged wind kinetic energy $(u^2+v^2)/2$ (units: m^2/s^2) and (b) zonal wind shear $\partial u/\partial y$ (units: s^{-1}) derived from the gridded RSS QuikSCAT product. The horizontal-dashed lines mark the boundary of the study region.

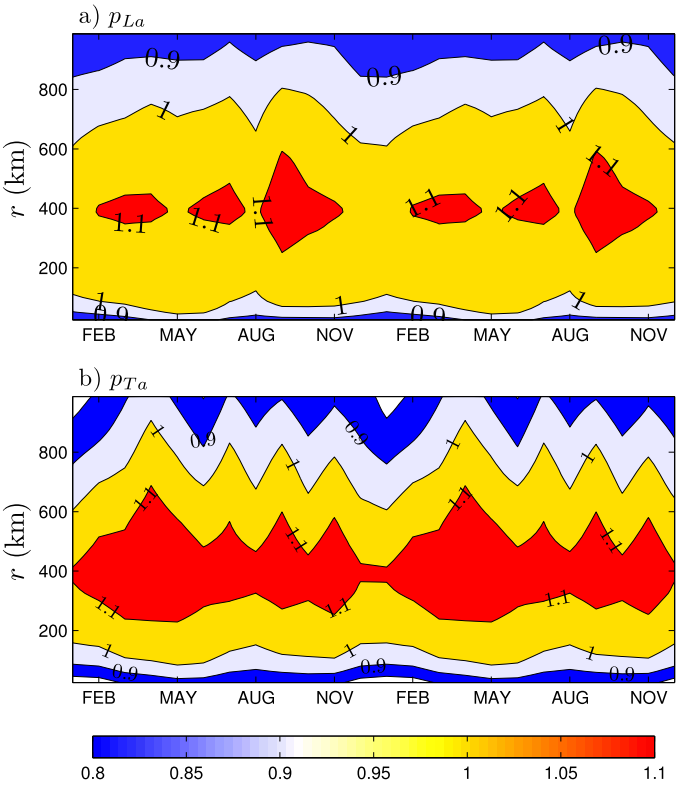

Figure 9. Seasonal variability of the spatial variance power law exponents for the Kuroshio Extension region as a function of r: (a) p_{La} and (b) p_{Ta}.

the zonal wind shear migrates north and reenters the study area; this produces a secondary maximum.

Figure 9 shows the seasonal cycle of the spatial variance slopes p_{La} and p_{Ta} and their dependence on r. The figure shows that seasonal variability is weak and close to 1 (corresponding to a spectral exponent of -2), consistent with spectral studies [*Patoux and Brown*, 2001; *Patoux et al.*, 2010; *Xu et al.*, 2011].

4.2.3. Interannual Variability

Figure 10 shows the interannual variability of the spatial variance (top) and dV/dr (middle and bottom). (A 13 month low-pass filter was applied to remove the seasonal cycle.) The interannual variability of V_{La} and V_{Ta} differs. The densities dV_{La}/dr and dV_{Ta}/dr are also compared with the regionally averaged wind speed and kinetic energy (figure not shown). A weak correlation is found between the kinetic energy and each *TKE* component, with

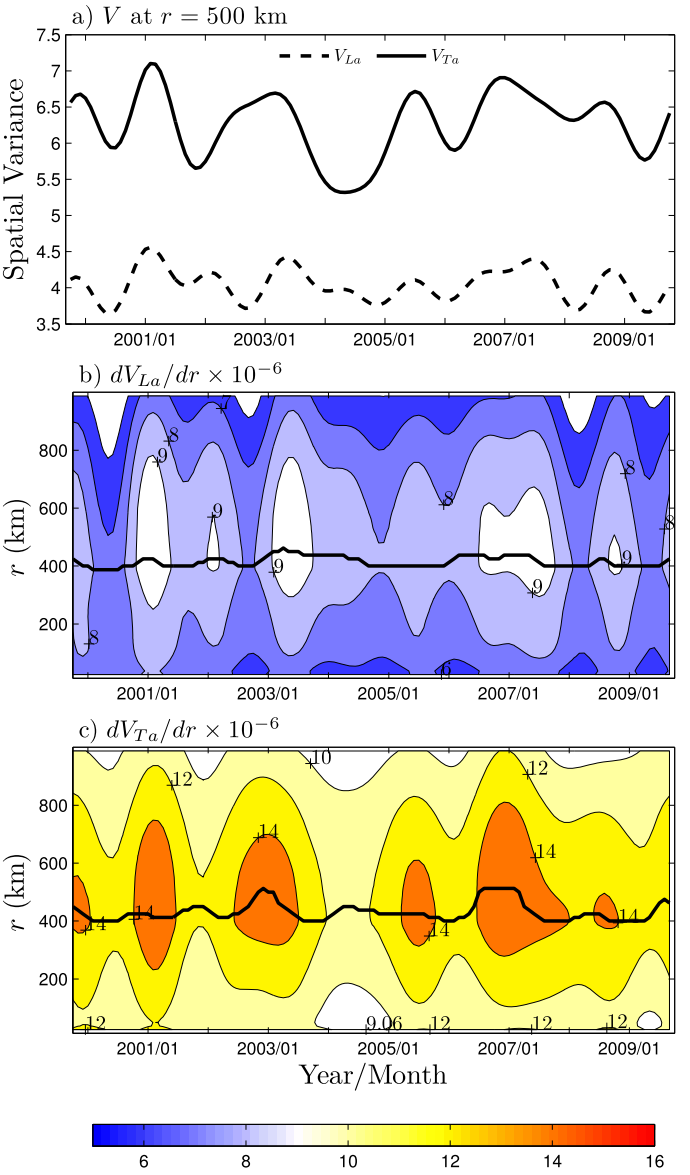

Figure 10. Interannual variability of the kinetic energy over the Kuroshio Extension: (a) spatial variance V at $r = 500$ km (units: m^2/s^2); spatial variance densities (b) dV_{La}/dr; and (c) dV_{Ta}/dr (units: m/s^2). The scale at which dV/dr is maximum is shown by the black line in Figures 10b and 10c.

correlation coefficients equal to about 0.5, which, however, is a little below the 95% confidence level.

Figure 11 shows the interannual variability of the scale-dependent slopes $p_{La}(r)$ and $p_{Ta}(r)$. Just as for the slopes for the mean state and the seasonal variability, the steepest slopes occur at about 400 km throughout the study period. Interestingly, at scales larger than 400 km the transverse slopes p_{Ta} are highly correlated with ENSO (Figure 12a). The correlation coefficient between $p_{Ta}(r)$ at scales between 500 and 700 km and the El Niño 3.4 index exceeds 0.75 (over 99% confidence level). Time series (normalized) of p_{La} and p_{Ta} between 500 and 700 km with the El Niño 3.4 index are shown in Figure 12b. The figure shows that both p_{La} and p_{Ta} are well-correlated with the El Niño index. The better correlation is with p_{Ta}. The strong correlation could be due to variability in the baroclinicity of the atmosphere. We discuss this speculation further in section 5.

4.3. Third-Order Statistics

The third-order structure function measures the asymmetry in the distribution of velocity increments. Thus if $D_{LLLa}(r)$ (or equivalently, $S_L(r)$) is negative, then convergence dominates over divergence. In the context of turbulence theory, $D_{LLLa}(r)$ is central to the question of whether energy is transferred upscale or downscale. The theory predicts that in the inertial range of 3-D turbulence, the third-order structure function is negative and linear in r. Figure 13a shows that $D_{LLLa}(r)$ is negative and linear out to about 300 km, turning to a positive slope after 700 km. Between about 50 and 300 km the slope is approximately -3×10^{-4} m^2s^{-3}, an order of magnitude larger than that estimated for the tropical Pacific by *King et al.* [2015b], but smaller than that estimated for the stratosphere by *Cho and Lindborg* [2001]. The theory also predicts that the skewness should be independent of r and approximately equal to -0.3. However, Figure 13b shows that the skewness S_{La} is far from constant, varying between -4 at small scales to about -0.3 or -0.4 at large scales. These results support an interpretation of downscale energy transfer for the Kuroshio Extension region, but the very large negative values at small r indicate strong scale interaction. There is not yet a theory for this behavior. However, a similar skewness characteristic was found by *King et al.* [2015b]: from visual inspection of QuikSCAT fields they associated the large negative skewness at small r with the passage of intense storms along the axis of the Intertropical Convergence Zone. This suggests that the large negative skewness seen in our results are due to the rapid growth of baroclinic instability over the Kuroshio extension. Indeed, several

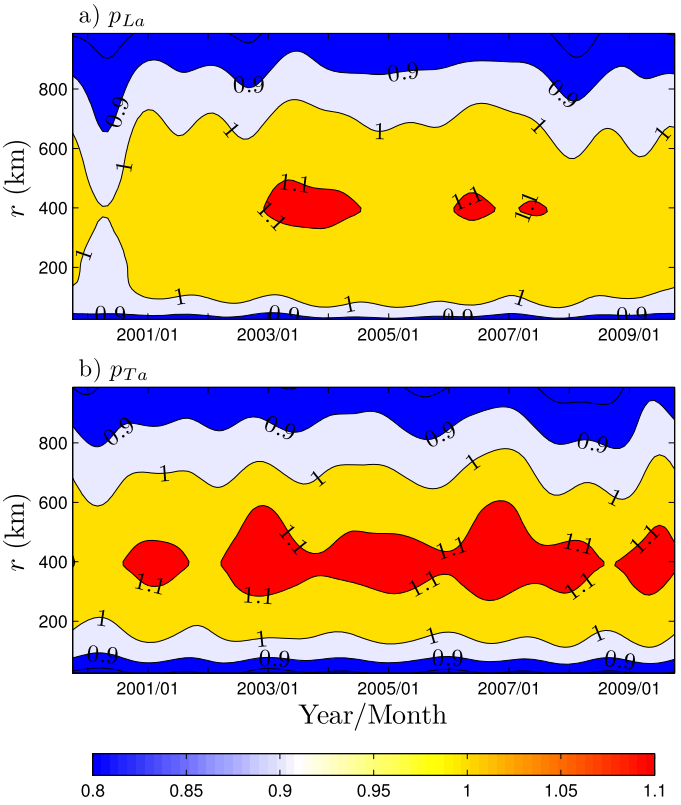

Figure 11. Interannual variability of the scale-dependent (a) longitudinal and (b) transverse slope for the spatial variance over the Kuroshio Extension region.

previous studies have identified global hot spots where explosive cyclogenesis (associated with the diabatic heating by invigorated convection as wintertime frontal systems bring cold air over the much warmer SSTs) rapidly increases the baroclinicity: The Kuroshio Current and Kuroshio Extension, the Gulf Stream, and off the eastern coasts of South America and Australia and New Zealand [*Black and Pezza*, 2013]. Furthermore, *Yoshiike and Kawamura* [2009] find evidence of the role of the East Asian monsoon on explosive cyclogenesis in the Kuroshio regions, and *Sakai and Kawamura* [2009] identify the influence of ENSO on the East Asian monsoon. Further work is needed to pin down the interpretation and connection of explosive cyclogenesis and the very large skewness found here.

The transverse third-order structure function has received virtually no attention in turbulence theory [but see *Deusebio et al.*, 2014], and yet it is of considerable geophysical interest as it measures the asymmetry in cyclonic/anticyclonic motion. Figure 13c shows that $D_{TTa}(r)$ is positive and linear out to about 300 km and then turns to a constant value near 600 km. The slope at small r (calculated between 50 and 300 km) is approximately 7.5×10^{-4} m^2s^{-3}. The transverse skewness S_{Ta} (Figure 13d) is, like the longitudinal skewness, strongly nonlinear—large magnitudes at small r and then decreases to between about 1 and 0.5 at large r. The large positive transverse skewness implies a preference for intense cyclonic motions—just as expected in a midlatitude stormy region.

The large-positive transverse skewness is consistent with results of an observational analysis of lower stratosphere data and numerical simulations reported by *Deusebio et al.* [2014]. In contrast to our results, these authors found an r^2 dependence at small r and an approximately constant skewness. The implication is that air-sea interaction is responsible for the difference.

Normally turbulence studies report a single value of the skewness. But this is an average. On monthly time scales there are fluctuations as we show in Figure 14. Here monthly time series for both S_{La} and S_{Ta} are shown at $r = 100$ km. The fluctuations are large and frequent, indicating significant intermittency.

Finally, it is interesting to compare the skewness from QuikSCAT winds with that from the NCEP winds. Figure 15 shows a scattergram of both longitudinal and transverse skewness at 50, 100, and 500 km. Note that for the Kuroshio Extension region, S_{La} is always negative and therefore lies wholly in the lower left quadrant, while S_{Ta} is always positive and lies wholly in the upper right quadrant. The figure shows that at large r QuikSCAT and NCEP longitudinal and transverse skewness are in very good agreement, but deteriorates as r decreases. The figure also shows an asymmetry: as r increases, the limiting value of the longitudinal skewness is closer to zero than the limiting value of the transverse skewness. Further work is necessary to determine if this asymmetry has any fundamental significance.

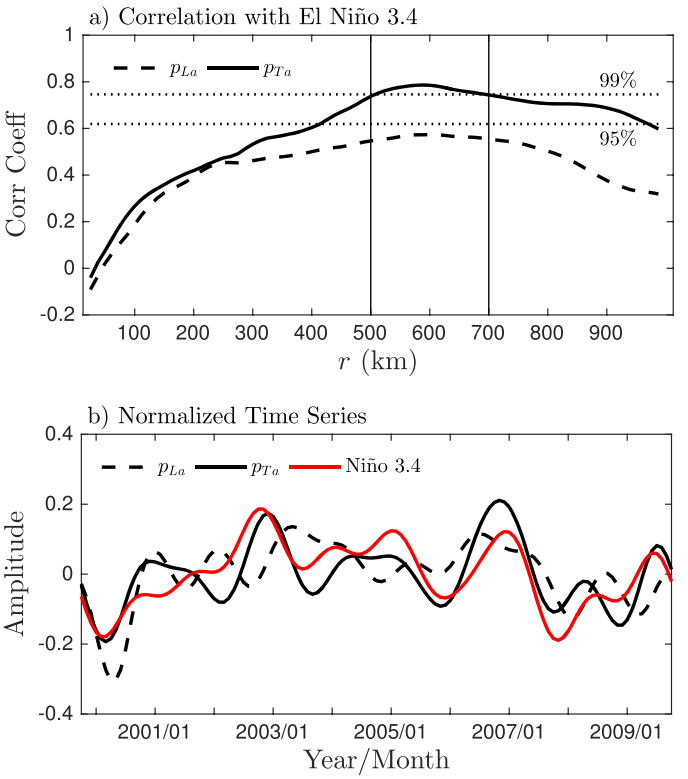

Figure 12. (a) The correlation at each scale r between the El Ni no 3.4 index and the spatial variance slopes p_{La} and p_{Ta}. The horizontal-dotted lines indicate the 95% and 99% confidence levels. (b) Interannual variability of the El Ni no 3.4 index compared with that for the slopes, using their mean values for the range 500–700 km (the range indicated by the vertical lines in Figure 12a).

5. Discussion and Conclusions

The Kuroshio Extension is thought to be the most energetic region in the world for both atmospheric and oceanic motions. The present studies use turbulence structure functions and spatial variance calculated using QuikSCAT winds for the 10 year period November 1999 through October 2009 to investigate the mesoscale (12.5–1000 km) *TKE* over the Kuroshio Extension region. Due to the sensitivity of Ku-band radar to rain, structure functions calculated from all-weather and rain-free winds were compared; the effects of rain were found to be small and only results for all-weather winds were reported.

Both the second-order structure function and the spatial variance provide measures of *TKE*. Formally the two are related, but the spatial variance has a higher tolerance for missing data and is statistically more robust at larger scales. Both measures follow a power law with an overall mean exponent of about 0.95. This is larger than predicted by classical turbulence theory, but consistent with previous scatterometer studies. The vorticity-to-divergence ratio was found to be about 1.5, midway between the 2-D and 3-D turbulence predictions. The ratio of the spatial variance and second-order structure function was found to be about 0.19, close to the predicted value.

The turbulent kinetic energy density shows a clear seasonal and interannual variability. The temporal variability at different scales is qualitatively the same and has a broad peak between about 400 and 500 km, which is of the same order as the Rossby deformation radius for midlatitudes—the preferred scale for baroclinic instability in midlatitudes.

The seasonal cycle, *TKE* higher in winter and lower in summer, is highly correlated with the seasonal variability of kinetic energy. The same seasonality was reported in the studies by *Patoux and Brown* [2001] and *Xu et al.* [2011] for their midlatitude results. Furthermore, *Xu et al.* [2011] report a steeper spectral slope in winter and a shallower slope in summer. They attribute this to the seasonal variability of energy input at the synoptic scale and transferred downscale. A similar seasonality was not found in our study for the spatial variance power law exponents.

In contrast to the seasonal variability, interannual variability shows clear differences between the longitudinal and transverse components of *TKE*. A weak correlation was found for both components of dV/dr and the regionally averaged kinetic energy. Finally, we found that the transverse spatial variance slope p_{Ta} correlates very well with the El Niño 3.4 index on interannual time scales. This can be explained as the result of increasing baroclinicity during El Niño years in the Kuroshio Extension [*Zhu and Sun*, 1999]: warm SST anomalies in the equatorial Pacific during an El Niño year increases the meridional SST gradient and potential energy, which in turn enhances baroclinicity in the midlatitudes. The increasing baroclinicity amplifies disturbances at the synoptic scale which then transfers downscale to the mesoscale through an energy-cascading process, making the spatial variance slope steeper.

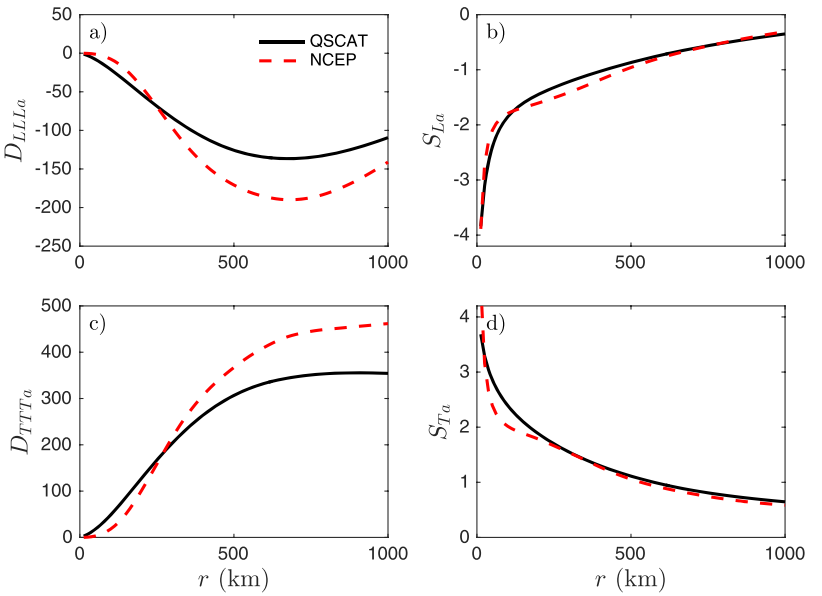

Figure 13. The third-order structure functions and skewness (for centered pdfs): (a) $D_{LLLa}(r)$; (b) $S_{La}(r)$; (c) $D_{TTTa}(r)$; and (d) $S_{Ta}(r)$. Note that throughout the range of scales, D_{LLLa} and S_{La} are always negative, while D_{TTTa} and S_{Ta} are always positive.

The present analysis has revealed significant temporal variability of *TKE* amplitude and power law exponents, and a correlation with surface wind kinetic energy, wind shear and the El Niño 3.4 index. Some of the results still lack an explanation. Further study of the temporal variability of the interactions of ocean wind turbulence with SST, SST fronts, and the free-tropospheric storm tracks is needed. Furthermore, the winds over the Kuroshio Extension are mainly zonal. Therefore, a study of the turbulent kinetic energy based on cross-track samples may reveal some additional interesting information.

The mean third-order longitudinal structure function $D_{LLLa}(r)$ was found to be negative and linear in r for scales out to about 300 km, turning to a positive slope after 700 km. Between about 50 and 300 km the

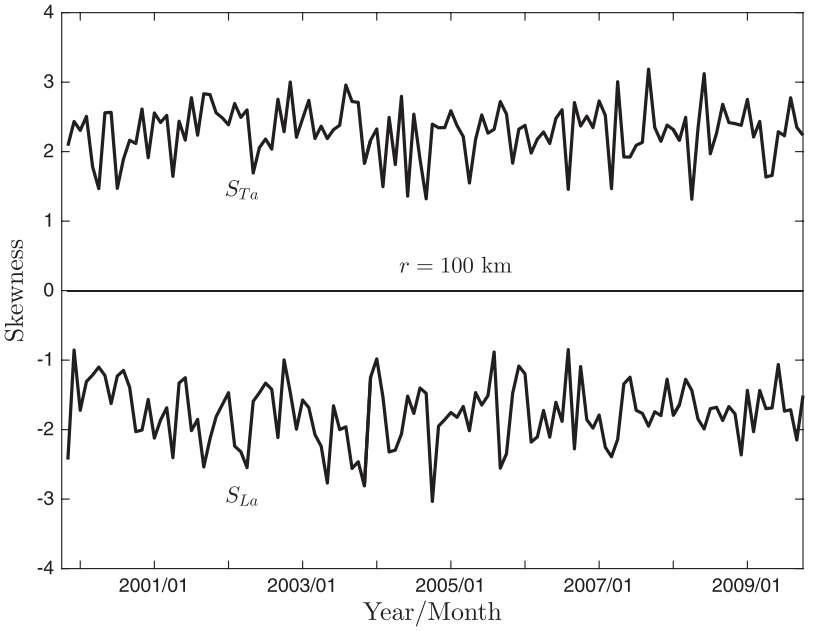

Figure 14. Fluctuations of the longitudinal S_{La} and transverse skewness S_{Ta} at $r = 100$ km.

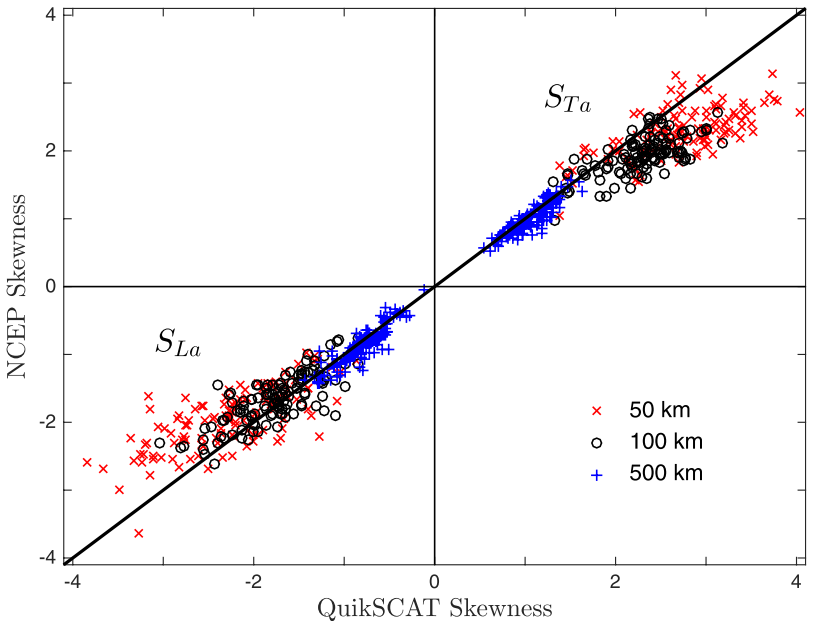

Figure 15. Scatter plot comparing QuikSCAT skewness with NCEP skewness using values at 50, 100, and 500 km. For the Kuroshio Extension region, S_{La} is always negative and therefore lies wholly in the lower left quadrant, while S_{Ta} is always positive and lies wholly in the upper right quadrant.

slope is approximately -3×10^{-4} m^2s^{-3}, an order of magnitude larger than estimated for the tropical Pacific by *King et al*. [2015b], but smaller than that estimated for the stratosphere by *Cho and Lindborg* [2001]. The skewness S_{La} is far from constant, varying between -4 at small-scales to about -0.3 or -0.4 at large-scales. These results support an interpretation of downscale energy transfer for the Kuroshio Extension region, but the very large negative values at small r (and the large month-to-month fluctuations) indicate strong-scale interaction. This means that the turbulence is not classical turbulence; there is not yet a theory for this behavior.

The transverse third-order structure function $D_{TTTa}(r)$, which measures the asymmetry in cyclonic/anticyclonic motion, was found to be positive and linear out to about 300 km, and then turned to a constant value near 600 km. The slope at small r (calculated between 50 and 300 km) was found to be approximately 7.5×10^{-4} m^2s^{-3}. The linear in r at small-scales distinguishes the surface wind third-order statistics from that found for the lower stratosphere by [*Deusebio et al*., 2014]. The transverse skewness S_{Ta} is, like the longitudinal skewness, strongly nonlinear—large magnitudes at small r and then a decrease to between about 1 and 0.5 at large r. The large positive transverse skewness implies a preference for intense cyclonic motions—just as expected along a storm track, and its strong month-to-month fluctuations at small r indicate strong-scale interaction and significant intermittency effects—characteristics which call out for new geophysical turbulence models.

Finally, a comparison between the monthly skewnesses calculated for QuikSCAT winds with those calculated using NCEP global forecast winds was summarized in a scattergram. The scattergram of skewnesses provides a new diagnostic to compare observations with numerical weather prediction which can motivate the development of new modeling to parameterize the extreme values of turbulent events (such as occur in explosive cyclogenesis) revealed by scatterometer winds for use in weather and climate models.

Appendix A: A Spatial Variance Validation Using Nonstationary fBM

In this appendix, we use nonstationary fractional Brownian motion (fBm) to show that equations (11) and (12) accurately describe the relationship between spatial variance (V) and the second-order structure function (D_2). An fBm algorithm is used to construct a time series with given power law characteristics: If we set the Hurst exponent [*Hurst*, 1951] to $H = 1/3$, a nonstationary fBm time series (Figure A1a) is produced such that the second-order structure function $D_2 \sim \tau^p$ follows a $p=2H=2/3$ power law (Figure A1b). Figure A1b

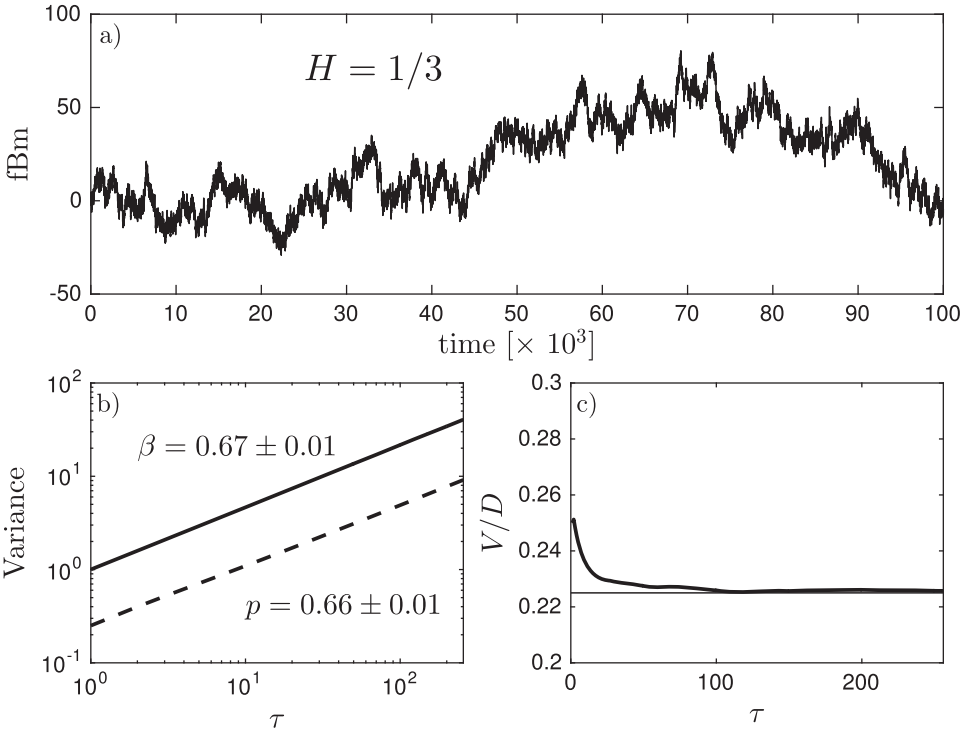

Figure A1. (a) A nonstationary fBm series simulated using a Hurst exponent $H = 1/3$. (b) Log-log plots of $D_2(\tau)$ (solid) and $V(\tau)$ (dashed), where τ is the increment. (c) The ratio $V(\tau)/D_2(\tau)$. At $\tau = 1$, $V/D_2 = 0.25$, and then decays toward the horizontal line located at $V/D_2 = 1/(p+1)(p+2) = 0.225$.

Acknowledgments
We thank Jur Vogelzang for his helpful comments and encouragement on the work. This research was supported by the National Key Research and Development Plan (grant 2016YFA0601800), National Science Foundation of China (grant 41606021, 41476022, and 41490643), Open Fund of State Key Laboratory of Satellite Ocean Environment Dynamics (grant QNHX1610), the Startup Foundation for Introducing Talent of NUIST (grant 2014r017, and 2014r072), the National Programme on Global Change and Air-Sea Interaction (grant GASI-03-IPOVAI-05), and the Priority Academic Program Development of Jiangsu Higher Education Institutions (PAPD). The QuikSCAT Level 2B Ocean Wind Vectors used here are the 12.5km Slice Composites Version 3. Ver. 3. PO.DAAC, CA, USA. Dataset accessed [21 September 2016] at https://doi.org/10.5067/QSX12-L2B01. QuikScat monthly gridded data used here are produced by Remote Sensing Systems and sponsored by the NASA Ocean Vector Winds Science Team. The monthly gridded QuikSCAT data sets are available at ftp://ftp.remss.com/qscat/bmaps_v04/. The fractional Brownian motion data was generated using a Matlab script written by Anders Holtsberg and available at http://se.mathworks.com/matlabcentral/newsreader/view_thread/16679.

also shows a log-log plot of the spatial variance. It is clear that the slopes of $D_2(\tau)$ and $V(\tau)$ are parallel. However, the magnitude of $V(\tau)$ is smaller. Figure A1c shows the ratio $V(\tau)/D_2(\tau)$ decays from an initial value of 0.25 at $\tau = 1$ (as expected for samples of length 2) down to $V/D_2 = 1/(p+1)(p+2) = 0.225$ for $p = 2/3$, just as predicted by equation (17). These results demonstrate the veracity of the derived spatial variance relationships.

References

Black, M. T., and A. B. Pezza (2013), A universal, broad-environment energy conversion signature of explosive cyclones, *Geophys. Res. Lett.*, *40*, 452–457, doi:10.1002/grl.50114.

Booth, J. F., L. A. Thompson, J. Patoux, K. A. Kelly, and S. Dickinson (2010), The signature of the midlatitude tropospheric storm tracks in the surface winds, *J. Clim.*, *23*(5), 1160–1174, doi:10.1175/2009JCLI3064.1.

Cho, J. Y. N., and E. Lindborg (2001), Horizontal velocity structure functions in the upper troposphere and lower stratosphere, 1. Observations, *J. Geophys. Res.*, *106*(D10), 10,223–10,232, doi:10.1029/2000JD900814.

Davidson, P. A., and B. R. Pearson (2005), Identifying turbulent energy distributions in real, rather than Fourier, space, *Phys. Rev. Lett.*, *95*, 214501, doi:10.1103/PhysRevLett.95.214501.

Deusebio, E., P. Augier, and E. Lindborg (2014), Third-order structure functions in rotating and stratified turbulence: A comparison between numerical, analytical and observational results, *J. Fluid Mech.*, *755*, 294–313, doi:10.1017/jfm.2014.414.

Fore, A., B. Stiles, A. Chau, B. Williams, R. Dunbar, and E. Rodríguez (2014), Point-wise wind retrieval and ambiguity removal improvements for the QuikSCAT climatological data set, *IEEE Trans. Geosci. Remote Sens.*, *52*(1), 51–59, doi:10.1109/TGRS.2012.2235843.

Frisch, U. (1995), *Turbulence: The legacy of A. N. Kolmogorov*, 296 pp., Cambridge Univ. Press, New York.

Hurst, H. (1951), Long-term storage capacity of reservoirs, *Trans. Am. Soc. Civ. Eng.*, *116*, 770–799.

Kelly, K. A., R. J. Small, R. M. Samelson, B. Qiu, T. M. Joyce, Y.-O. Kwon, and M. F. Cronin (2010), Western boundary currents and frontal air–sea interaction: Gulf stream and Kuroshio extension, *J. Clim.*, *23*(21), 5644–5667, doi:10.1175/2010JCLI3346.1.

King, G. P., J. Vogelzang, and A. Stoffelen (2015a), Second-order structure function analysis of scatterometer winds over the tropical pacific, *J. Geophys. Res. Oceans*, *120*, 362–383, doi:10.1002/2014JC009992.

King, G. P., J. Vogelzang, and A. Stoffelen (2015b), Upscale and downscale energy transfer over the tropical Pacific revealed by scatterometer winds, *J. Geophys. Res. Oceans*, *120*, 346–361, doi:10.1002/2014JC009993.

Lindborg, E. (1999), Can the atmospheric kinetic energy spectrum be explained by two-dimensional turbulence?, *J. Fluid Mech.*, *388*, 259–288, doi:10.1017/S0022112099004851.

Lindborg, E. (2007), Horizontal wavenumber spectra of vertical vorticity and horizontal divergence in the upper troposphere and lower stratosphere, *J. Atmos. Sci.*, *64*(3), 1017–1025, doi:10.1175/JAS3864.1.

Patoux, J., and R. A. Brown (2001), Spectral analysis of QuikSCAT surface winds and two-dimensional turbulence, *J. Geophys. Res.*, *106*(D20), 23,995–24,005, doi:10.1029/2000JD000027.

Patoux, J., R. C. Foster, and R. A. Brown (2010), A method for including mesoscale and synoptic-scale information in scatterometer wind retrievals, *J. Geophys. Res.*, *115*, D11105, doi:10.1029/2009JD013193.

Qiu, B. (1995), Variability and energetics of the Kuroshio extension and its recirculation gyre from the first two-year topex data, *J. Phys. Oceanogr.*, *25*(8), 1827–1842, doi:10.1175/1520-0485(1995)025 < 1827:VAEOTK>2.0.CO;2.

Qiu, B. (2000), Interannual variability of the Kuroshio extension system and its impact on the wintertime SST field, *J. Phys. Oceanogr.*, *30*(6), 1486–1502, doi:10.1175/1520-0485(2000)030 < 1486:IVOTKE>2.0.CO;2.

Ricciardulli, L., F. Wentz, and D. Smith (2011), *Remote Sensing Systems Quikscat Ku-2011 Monthly Ocean Vector Winds on 0.25° Grid, Version 4*, Remote Sens. Syst., Santa Rosa, Calif. [Available at www.remss.com/missions/qscat.]

Sakai, K., and R. Kawamura (2009), Remote response of the East Asian winter monsoon to tropical forcing related to El Niño Southern Oscillation, *J. Geophys. Res.*, *114*, D06105, doi:10.1029/2008JD010824.

Tai, C.-K., and W. B. White (1990), Eddy variability in the Kuroshio extension as revealed by Geosat altimetry: Energy propagation away from the jet, Reynolds stress, and seasonal cycle, *J. Phys. Oceanogr.*, *20*(11), 1761–1777, doi:10.1175/1520-0485(1990)020 < 1761:EVITKE>2.0.CO;2.

Tanimoto, Y., S.-P. Xie, K. Kai, H. Okajima, H. Tokinaga, T. Murayama, M. Nonaka, and H. Nakamura (2009), Observations of marine atmospheric boundary layer transitions across the summer Kuroshio extension, *J. Clim.*, *22*(6), 1360–1374, doi:10.1175/2008JCLI2420.1.

Tokinaga, H., Y. Tanimoto, M. Nonaka, B. Taguchi, T. Fukamachi, S.-P. Xie, H. Nakamura, T. Watanabe, and I. Yasuda (2006), Atmospheric sounding over the winter Kuroshio Extension: Effect of surface stability on atmospheric boundary layer structure, *Geophys. Res. Lett.*, *33*, L04703, doi:10.1029/2005GL025102.

Tsai, W.-T., M. Spencer, C. Wu, C. Winn, and K. Kellogg (2000), SeaWinds on QuikSCAT: Sensor description and mission overview, International Geoscience and Remote Sensing Symposium 2000, in *Proceedings IGARSS 2000*, vol. 3, pp. 1021–1023, IEEE 2000 International, doi:10.1109/IGARSS.2000.858008.

Vogelzang, J. and A. Verhoef (2014), The orientation of SeaWinds wind vector cells, *Tech. Rep.*, *NWPSAF-KN-TR-003*, European Organisation for the Exploitation of Meteorological Satellites (EUMETSAT), KNMI, De Bilt, Netherlands. [Available at http://nwpsaf.eu/publications/tech_reports/nwpsaf-kn-tr-003.pdf.]

Vogelzang, J., A. Stoffelen, A. Verhoef, and J. Figa-Saldana (2011), On the quality of high-resolution scatterometer winds, *J. Geophys. Res.*, *116*, C10033, doi:10.1029/2010JC006640.

Vogelzang, J., G. P. King, and A. Stoffelen (2015), Spatial variances of wind fields and their relation to second-order structure functions and spectra, *J. Geophys. Res. Oceans*, *120*, 1048–1064, doi:10.1002/2014JC010239.

Vogelzang, J., A. Stoffelen, R. D. Lindsley, A. Verhoef, and J. Verspeek (2016), The ASCAT 6.25-km wind product, *IEEE J. Sel. Top. Appl. Earth Observ. Remote Sens.*, (99), 1–11, doi:10.1109/JSTARS.2016.2623862.

Weissman, D. E., B. W. Stiles, S. M. Hristova-Veleva, D. G. Long, D. K. Smith, K. A. Hilburn, and W. L. Jones (2012), Challenges to satellite sensors of ocean winds: Addressing precipitation effects, *J. Atmos. Oceanic Technol.*, *29*(3), 356–374, doi:10.1175/JTECH-D-11-00054.1.

Wyrtki, K., L. Magaard, and J. Hager (1976), Eddy energy in the oceans, *J. Geophys. Res.*, *81*(15), 2641–2646, doi:10.1029/JC081i015p02641.

Xu, Y., L.-L. Fu, and R. Tulloch (2011), The global characteristics of the wavenumber spectrum of ocean surface wind, *J. Phys. Oceanogr.*, *41*, 1576–1582, doi:10.1175/JPO-D-11-059.1.

Yoshiike, S., and R. Kawamura (2009), Influence of wintertime large-scale circulation on the explosively developing cyclones over the western North Pacific and their downstream effects, *J. Geophys. Res.*, *114*, D13110, doi:10.1029/2009JD011820.

Yu, L., and R. A. Weller (2007), Objectively analyzed air–sea heat fluxes for the global ice-free oceans (1981–2005), *Bull. Am. Meteorol. Soc.*, *88*(4), 527–539, doi:10.1175/BAMS-88-4-527.

Zhu, W., and Z. Sun (1999), Influence of Enso event on the maintenance of pacific storm track in the northern winter, *Adv. Atmos. Sci.*, *16*(4), 630–640, doi:10.1007/s00376-999-0037-9.